PHILOSOPHICAL TRANSACTIONS OF THE ROYAL SOCIETY B BIOLOGICAL SCIENCES

The three–dimensional leading–edge vortex of a 'hovering' model hawkmoth

Coen Van den berg and Charles P. Ellington

Phil. Trans. R. Soc. Lond. B 1997 **352**, 329-340
doi: 10.1098/rstb.1997.0024

The three-dimensional leading-edge vortex of a 'hovering' model hawkmoth

COEN VAN DEN BERG* AND CHARLES P. ELLINGTON

Department of Zoology, University of Cambridge, Downing Street, Cambridge CB2 3EJ, UK

CONTENTS

SUMMARY

Recent flow visualization experiments with the hawkmoth, *Manduca sexta*, revealed a small but clear leading-edge vortex and a pronounced three-dimensional flow. Details of this flow pattern were studied with a scaled-up, robotic insect ('the flapper') that accurately mimicked the wing movements of a hovering hawkmoth. Smoke released from the leading edge of the flapper wing confirmed the existence of a small, strong and stable leading-edge vortex, increasing in size from wingbase to wingtip. Between 25 and 75% of the wing length, its diameter increased approximately from 10 to 50% of the wing chord. The leading-edge vortex had a strong axial flow velocity, which stabilized it and reduced its diameter. The vortex separated from the wing at approximately 75% of the wing length and thus fed vorticity into a large, tangled tip vortex. If the circulation of the leading-edge vortex were fully used for lift generation, it could support up to two-thirds of the hawkmoth's weight during the downstroke. The growth of this circulation with time and spanwise position clearly identify dynamic stall as the unsteady aerodynamic mechanism responsible for high lift production by hovering hawkmoths and possibly also by many other insect species.

1. INTRODUCTION

Willmott *et al.* (1997) discovered a leading-edge vortex on the wings of the hawkmoth, *Manduca sexta*, which increased in size from wingbase to tip. The vortex was small at low flight speeds, but increased in size with speed until it extended across the whole wing. This is the best evidence yet for the existence of the lift-enhancing leading-edge vortex that is expected for insect flight. Van den Berg & Ellington (1997) also found a leading-edge vortex on a 'hovering' model hawkmoth (the 'flapper'), in good qualitative agreement with the *Manduca* results. A strong axial flow velocity stabilized the vortex and kept it quite small. At approximately three-quarters of the wing length it separated from the wing surface and blended into a wide, tangled tip vortex, which connected to a combined stopping/starting vortex from pronation. In this manner, a roughly ring-shaped vortex wake was generated by each wing during the downstroke. An estimate of the impulse of the downstroke wake confirmed that this flow pattern provides the lift required for weight support (Van den Berg & Ellington 1997).

* Current address: Faculty of Human Movement Sciences, Vrije Universiteit, Van der Boechorststraat 9, 1081 BT, Amsterdam, The Netherlands.

The most important outstanding problem is which of two aerodynamic mechanisms is responsible for generation of the leading-edge vortex. If a rotational lift mechanism is involved, the leading-edge vortex is shed during pronation and recaptured at the start of the downstroke; under these conditions the circulation should be proportional to the square of wing chord, c. However, if the vortex is generated by dynamic stall, the circulation should start to build up at the start of the downstroke and should be proportional to the product of c and spanwise position, r (Ellington 1984). Dynamic stall is the mechanism by which a wing operates above the stall angle and temporarily increases its lift. Willmott *et al.* (1997) could not resolve the issue because the early stage of vortex formation was unclear. However, by carefully studying the characteristics of the leading-edge vortex with the flapper, it should be possible to distinguish between the two mechanisms of vortex generation. Therefore, in this paper we elaborate on the size, development and strength of the three-dimensional leading-edge vortex during simulated hawkmoth hovering.

2. MATERIALS AND METHODS

(*a*) *The flapper*

The leading-edge vortex was studied using a robotic insect (the 'flapper') which can mimic the movements of insect wings during flapping flight. The flapper and the experimental methods are described in detail in Van den Berg & Ellington (1997); only an outline is presented here. Each wing has a forewing and hindwing section, which can twist independently. This construction represents a functionally two-winged insect. The wings of the flapper have four degrees of freedom (figure 1): the positional angle, ϕ, the elevation angle, θ, and the angle of attack of the leading-edge section, α_l, and the trailing-edge section, α_t, near the wing-base. The wings were constructed such that they produce a realistic cambered and twisted wing profile during both the upstroke and the downstroke. Smoke (vaporized oil) was released from a smoke rake built into the leading edge of the right wing. The wing movements of the flapper were controlled with a Macintosh Quadra 650 computer, using a LabView 3.0 program. The wing movements were based on detailed measurements of the wing kinematics of a hovering hawkmoth, *Manduca sexta*, in one high-speed video sequence (Willmott 1995; Van den Berg & Ellington 1997). The hawkmoth in this sequence was a male with a body mass of 1.58 g, a wing length, R, of 4.85 cm and a wingbeat frequency of 26.1 s^{-1}. The flapper, with a wing length of 46.5 cm, was scaled up by a factor of 9.6. For aerodynamic similarity it had to be operated at the same Reynolds number as the hovering hawkmoth, giving a wingbeat frequency of 0.30 s^{-1}.

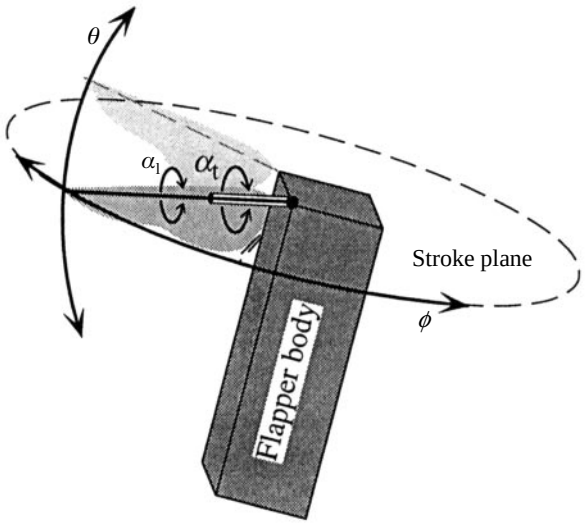

Figure 1. The four degrees of freedom of the right wing of the flapper. Note that the stroke plane angle of the hovering hawkmoth is 15°. The wings can flap in the stroke plane (ϕ) and move perpendicular to it (θ). Furthermore, the leading- and trailing-edge sections of each wing can twist independently ($\alpha_{l,t}$), since they are mounted on coaxial axes.

(*b*) *Measurement of the vortex dimensions and position*

The flapper was filmed with a Hitachi CCTV video camera (WV-BL600/B), with a Fujinon zoom lens (1:1.2/12.5–75) and a Panasonic NV-J35B video recorder. The smoke used for flow visualization was an oil vapour, produced with an FVSP/E smoke generator (Nutem Ltd) and a medicinal white oil (Shell Ondina EL).

For measurements of the leading-edge vortex the flapper was filmed in a side view. Most video recordings used for analysis employed a 'light slice' to illuminate a cross-section of the flow. The camera was positioned such that, at a predetermined positional angle of the wing, the wing axis was exactly perpendicular to the image plane. The leading-edge vortex was analysed in the video frame closest to that position. The spanwise position of interest was lit by an Arri 'junior' 1000 W manual spotlight with almost closed barn doors, giving a slit of light approximately 7 cm wide and parallel to the image plane of the camera. Flow cross-sections were recorded at four positional angles of the wing ($\phi = 50, 30, 0$ and $-36°$), and for each positional angle at up to five spanwise positions along the wing ($0.25R$, $0.50R$, $0.63R$, $0.75R$, $0.87R$). At the start of each experiment, a ruler was filmed to calibrate scaling; the scaling factor was accurate to within 3%.

At each measurement site ten video frames (from ten different wingbeats) were digitized using Neotech Imagegrabber-24 on a Macintosh Quadra 650 computer. The vortex parameters (see below) were measured in these frames using NIH Image. The mean and 95% confidence intervals of each set of ten measurements were calculated using Statview® SE+.

In each digitized video frame the size, direction and/or position were recorded of the wing cross-section, the leading-edge vortex and the attachment streaklines (figure 2). For the wing cross-section we measured the leading- and trailing-edge sections, $C_{l,t}$, the angles of attack, $\alpha_{l,t}$, of those sections, and the angle of attack, α_w, of the wing measured between the stroke plane and the line connecting the leading edge and the

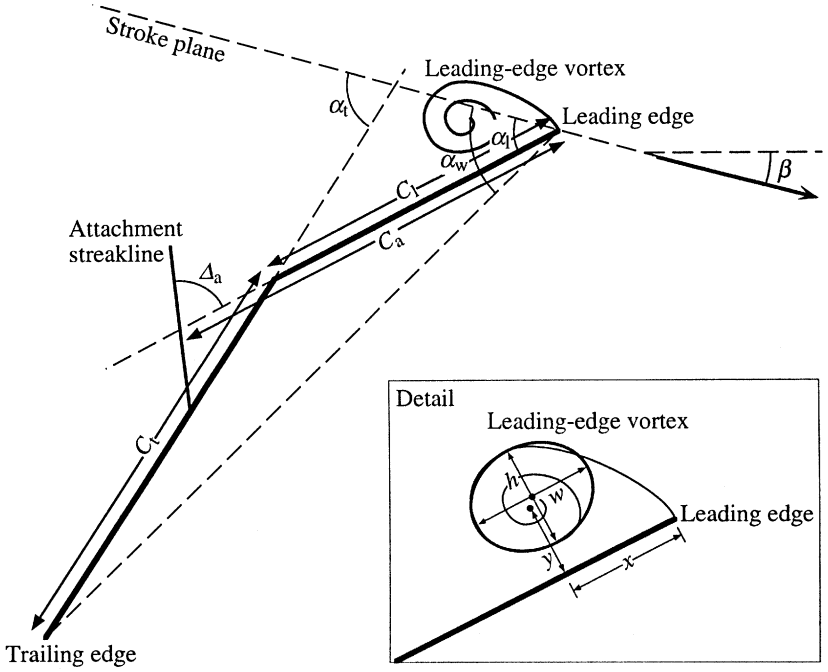

Figure 2. Schematic cross-section of the flapper wing during the downstroke. The parameters that were used to quantify the position and orientation of the wing cross-section, and the attachment streaklines are indicated (main figure), as well as the parameters that describe the leading-edge vortex (detail). C_a is the distance between the leading edge and the intersection of the attachment streakline with the (projected) leading-edge section; $C_{l,t}$ is the length of the leading-/trailing-edge section; h is the height (perpendicular to the leading-edge section) of the leading-edge vortex; x is the distance (parallel to the leading-edge section) between the aerodynamic centre of the leading-edge vortex and the leading edge; w is the width (parallel to the leading-edge section) of the leading-edge vortex; y is the perpendicular distance between the aerodynamic centre of the leading-edge vortex and the leading-edge section; $\alpha_{l,t}$ is the angle of attack of the leading-/trailing-edge section; α_w is the angle of attack of the line connecting the leading and trailing edges; β is the stroke plane angle; Δ_a is the angle between an attachment streakline and the (projected) leading-edge section.

trailing edge. The bend between the leading- and trailing-edge sections was usually smooth (e.g. figure 5); for analysis, lines were fitted through each section guided by the straight regions near the wing edge. For the leading-edge vortex we estimated the position of the aerodynamic centre of the vortex, and measured its perpendicular distance, y, from the forewing section and its distance, x (parallel to the forewing section), from the leading edge. For analysis, the spiralling shape of the vortex was represented as an ellipse, parallel to the forewing section: the width, w, and height, h, were recorded. The aerodynamic centre of the vortex was usually slightly displaced from the geometric centre of the ellipse. The position of attachment streaklines was inferred from smoke streaklines ending at the wing surface. Sometimes, two distinct attachment streaklines could be observed. We measured the angle Δ_a between such streaklines and the (projected) forewing section, and the distance C_a between the leading edge and the point where the streaklines touched the (projected) forewing section. All angles were measured to $\pm 0.5°$ and distances to ± 0.1 cm.

(*c*) *Measurement of the axial flow velocity of the vortex*

The flow velocity within the leading-edge vortex can be separated into swirl (V_θ, the speed of rotation around the vortex axis), axial flow (V_a, the velocity parallel to the vortex axis), and radial flow perpendicular to the vortex axis (which proved to be negligible). The circulation of the leading-edge vortex, Γ_{le}, is determined by its swirl. Unfortunately, the swirl could not be measured because smoke quickly moved out of the cross-sections, due to the strong axial flow. However, the axial flow component could be measured, using the following method. The flapper was filmed in a top view, perpendicular to the leading edge and approximately parallel to the wing surface during the downstroke. The wing surface was illuminated from the side with an Arri 'junior' 1000 W spotlight. Except for its most basal part, the leading-edge smoke rake was closed off. At the start of the downstroke, some smoke was released manually, during a fraction of a second, resulting in a discrete 'smoke blob' at the base of the wing. Such a blob would spiral along the leading edge towards the wingtip, and its movement could be traced in 11 video sequences. The magnitude of the axial velocity was calculated from these sequences. The helix angle of the leading-edge vortex was estimated using top view photographs (e.g. figure 3*c*, 3*d*). Using simple goniometry, the swirl could be calculated from this helix angle and the axial flow velocity.

3. RESULTS

(*a*) *The leading-edge vortex*

The flow visualization experiments revealed a clear leading-edge vortex (figures 3, 4) with a large axial velocity component (figure 3*c*, 3*d*). Two attachment streamlines (on the upper and lower wing surface) divided the free flow around the wing from the flow into the leading-edge vortex (Van den Berg & Ellington 1997); the upper attachment is sometimes visible in figure 4 (marked 'as'). The air in between those streamlines rolled up into the leading-edge vortex and spiralled towards the wingtip. During the first half of the downstroke the vortex was stable over the whole wingspan (figure 3*a*), although stability varied between wingbeats (compare figure 3*a*, *c* and *d*). Towards the wingtip the stability of the vortex core decreased. During the second half of the downstroke, the vortex became unstable and detached from the wing surface between 0.63 *R* and 0.75 *R*; it subsequently connected to a large tip vortex with a broken down vortex core (details of the structure of the vortex wake are given in Van den Berg & Ellington (1997)). A similar, but smaller, leading-edge vortex was present during the upstroke. We only analysed the leading-edge vortex of the downstroke.

(*b*) *The size of the leading-edge vortex*

No leading-edge vortex had formed at $\phi = 50°$, just after wing pronation (at $\phi = 51°$).

A clear leading-edge vortex was present at $\phi = 30°$ (figures 4, 5*a*). Its height increased from 1 to 3.5 cm between 0.25 *R* and 0.63 *R*, and then remained constant. Its shape changed from oval ($w/h \approx 1.5$) at 0.25 *R* to circular ($w/h \approx 1$) at 0.63 *R* and 0.75 *R* (table 1). From wingbase to wingtip, the centre of the vortex moved away from the wing surface (from 0.6 to 2.7 cm) and chordwise back from the leading edge (from 1.5 to 3 cm). Clear attachment streaklines were visible with, from base to tip, an increasing angle to the wing surface.

At $\phi = 0°$ the leading-edge vortex had grown considerably (figures 4, 5*b*). The vortex height increased from 1.5 cm at 0.25 *R* to 7 cm at 0.75 *R*. The vortex shape changed from oval ($w/h \approx 1.4$) at 0.25 *R*

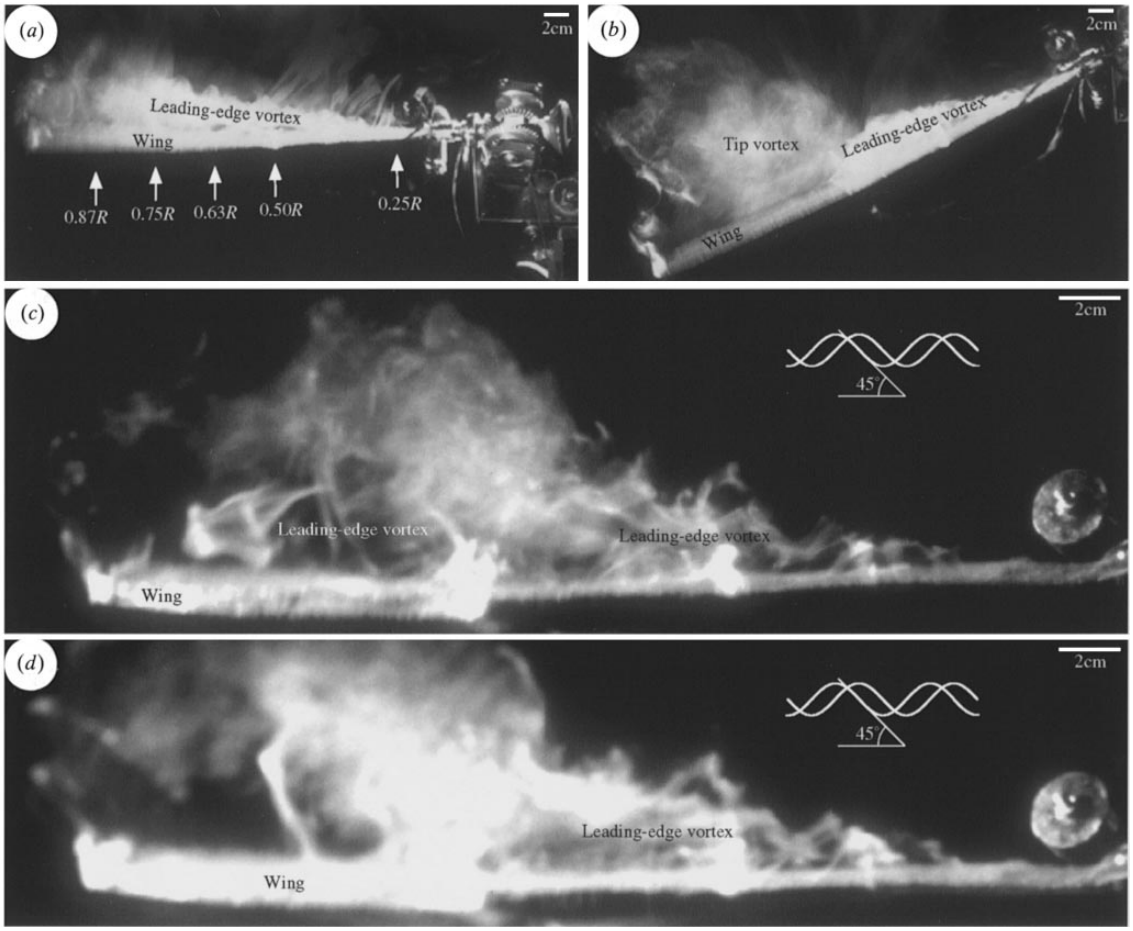

Figure 3. Flow visualization of the leading-edge vortex during the downstroke. The point of view is parallel to the wing surface, which approximately corresponds to a top view of the hovering hawkmoth. (*a*) The leading-edge vortex at $\phi = 0°$. In this image, some of the mechanical components of the flapper can be seen. The spanwise positions where the measurements were taken (see figures 4, 5) are indicated. (*b*) The leading-edge vortex at $\phi \approx -25°$. The development of a large, tangled tip vortex at approximately three-quarters of the wing length is very clear in this image. (*c*), (*d*) In these enlarged images of the leading-edge vortex at $\phi = 0°$ (compare with (*a*)), individual streaklines were observed in the smoke emitted from the leading edge. Using these spiralling streaklines, the helix angle of the leading-edge vortex was estimated to be approximately 45°. For comparison, a double helix with a helix angle of 45° is shown.

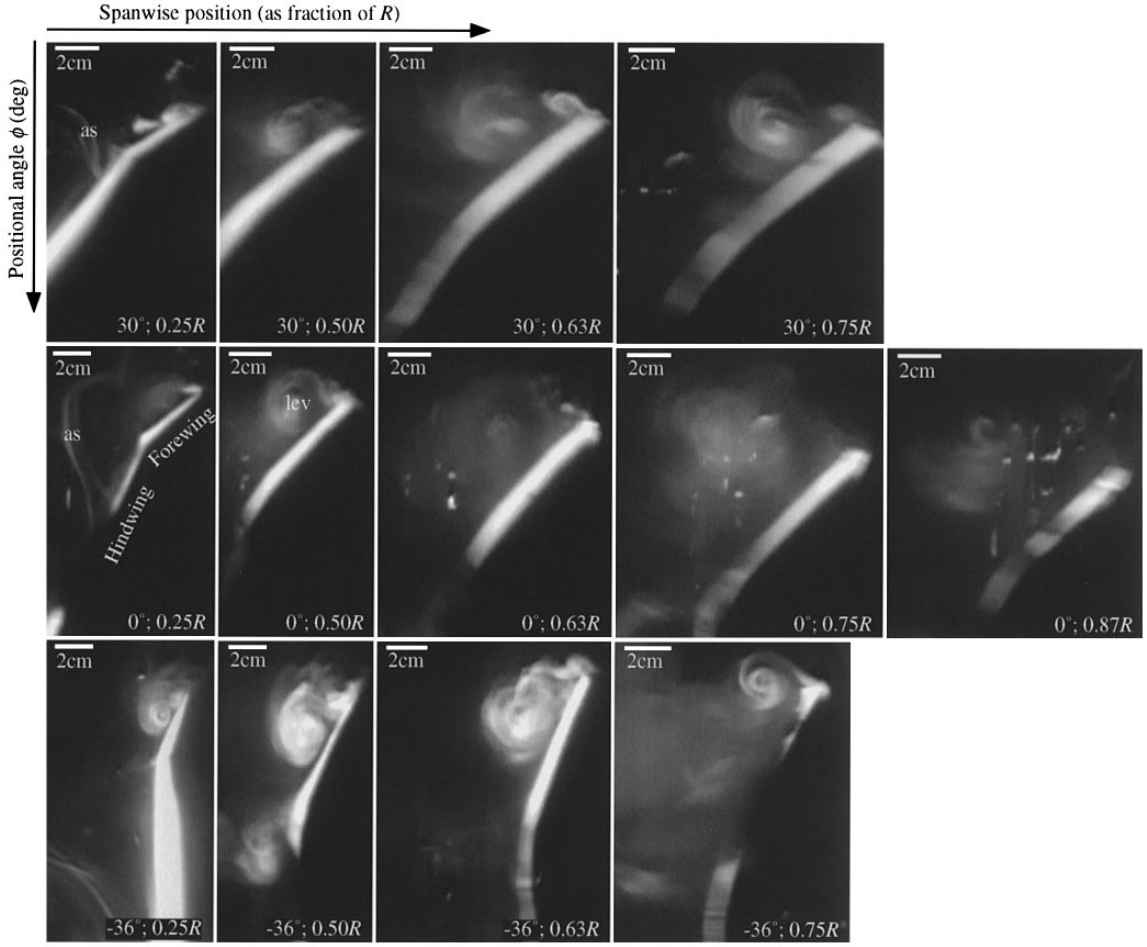

Figure 4. Cross-sections of the leading-edge vortex (taken from video recordings) are shown for three positional angles of the wing (from top to bottom: $\phi = 30$, 0 and $-36°$), at up to five spanwise positions along the wing (from left to right: $0.25R$, $0.50R$, $0.63R$, $0.75R$ and $0.87R$). The stroke plane in these images is horizontal. The smoke streaklines which join the wing surface are interpreted as attachment streaklines (as). The leading- and trailing-edge sections do not bend smoothly at the base of the wing ($0.25R$, $0.50R$). The sharp bend in the profile occasionally generated a secondary flow separation (e.g. at $0.50R$, $\phi = -36°$). In the spanwise series at $\phi = 0°$, one can clearly observe the gradual separation of the leading-edge vortex and the associated loss of coherence (at $0.75R$ and $0.87R$). At $0.75R$, $\phi = -36°$, the leading-edge vortex had separated and moved towards the trailing edge, while a new, small leading-edge vortex had formed close to the leading edge.

to circular ($w/h \approx 1$) at $0.75R$ and $0.87R$ (table 1). Between $0.25R$ and $0.63R$, the vortex remained close to the wing surface, but then separation started and the vortex moved away rapidly at $0.75R$ and $0.87R$. The distance between the vortex centre and the leading edge increased roughly from 2 cm ($0.25R$), to 3 cm ($0.50R$), to 4 cm ($0.63R$, $0.75R$ and $0.87R$). Attachment streaklines were only observed at $0.25R$ and $0.50R$, with a fairly shallow angle to the wing surface. The double attachment streaklines at $0.25R$ may be explained by the sharp bend in the wing profile at this position (figure 4), which may have caused a secondary flow separation (not visible) at the bend and an associated reattachment close downstream.

At $\phi = -36°$ (the onset of supination) the wing was decelerating with an angle of attack α_w close to 90° (figures 4, 5*c*). Compared with $\phi = 0°$ (figure 5*b*), the vortex height decreased by 10–20% between $0.25R$ and $0.63R$. The vortex shape changed from oval ($w/h \approx 1.3$) at $0.25R$ to circular ($w/h \approx 1$) at $0.63R$ and $0.75R$ (table 1). Between $0.25R$ and $0.63R$ the vortex remained close to the wing surface and its centre moved chordwise from 2 to 4 cm back from the leading edge. Between $\phi = 0°$ and $\phi = -36°$ a distal portion of the leading-edge vortex (starting between $0.63R$ and $0.75R$) separated from the wing surface and was immediately replaced by a new vortex (figure 4), which, at $0.75R$, was smaller (height 2.5 cm) and 2.5 cm closer to the leading edge (chordwise distance 1.5 cm) than the vortex at $0.63R$. Hence, it is probably not connected to the older part of the leading-edge vortex, extending towards the wingbase (figure 5*c*, plan view). No attachment streaklines were observed.

(*c*) *The axial flow velocity of the leading-edge vortex*

The mean axial flow velocity V_a (= flow component along the vortex axis) of the leading-edge vortex was 31.8 cm s^{-1}, with a fairly large variation depending on the spanwise position on the wing (figure 6). Mean axial velocities were calculated for four spanwise sections, corresponding to the $0.25R$, $0.50R$, $0.63R$ and $0.75R$ measurement sites (figure 6, table 2). The axial

Table 1. *Mean values and 95% confidence intervals of the parameters describing the shape and position of the wing cross-section, the leading-edge vortex and the attachment streaklines. The values are given for up to five spanwise cross-sections of the wing at each of four positional angles during the downstroke. For abbreviations, see figure 2*

ϕ	50°					30°			
r	0.25 R	0.50 R	0.63 R	0.75 R		0.25 R	0.50 R	0.63 R	0.75 R
α_1 (°)	93.1 ± 1.8	94.1 ± 2.4	98.8 ± 3.8	83.1 ± 3.8		30.9 ± 1.3	37.4 ± 0.6	38.5 ± 0.64	36.8 ± 1.3
α_t (°)	95.9 ± 1.2	95.8 ± 2.0	99.4 ± 1.8	92.5 ± 1.1		51.1 ± 1.5	57.4 ± 0.9	57.8 ± 1.21	61.7 ± 2.9
α_w (°)[a]	94.8	95.1	99.1	85.0		46.9	49.7	45.8	41.9
C_1 (cm)	7.22 ± 1.26	7.59 ± 0.13	7.10 ± 1.89	9.05 ± 0.20		3.87 ± 0.20	7.51 ± 0.38	8.69 ± 0.37	9.63 ± 0.44
C_t (cm)				2.34 ± 0.26		14.37 ± 0.15	11.88 ± 0.33	5.31 ± 0.34	2.55 ± 0.47
y (cm)						0.62 ± 0.10	1.53 ± 0.19	2.38 ± 0.20	2.66 ± 0.23
x (cm)						1.51 ± 0.27	2.57 ± 0.23	3.33 ± 0.48	3.05 ± 0.21
w (cm)						1.53 ± 0.11	2.50 ± 0.25	3.62 ± 0.25	3.50 ± 0.49
h (cm)						1.04 ± 0.08	2.25 ± 0.20	3.55 ± 0.36	3.67 ± 0.58
w/h						1.48 ± 0.18	1.11 ± 0.05	1.03 ± 0.06	0.97 ± 0.08
Δ_a (°)						99.1 ± 13.1	111.0 ± 6.8	139.2 ± 10.3	126.7 ± 11.3
C_a (cm)						6.15 ± 0.84	7.42 ± 0.63	5.80 ± 1.27	7.54 ± 1.33

ϕ	0°					−36°			
r	0.25 R	0.50 R	0.63 R	0.75 R	0.87 R	0.25 R	0.50 R	0.63 R	0.75 R
α_1 (°)	38.2 ± 0.6	42.8 ± 0.5	45.0 ± 0.7	45.8 ± 1.54	40.7 ± 0.9	62.7 ± 3.0	63.7 ± 0.9	66.2 ± 1.5	66.7 ± 2.3
α_t (°)	62.5 ± 0.6	73.3 ± 1.1				90.4 ± 1.9	98.2 ± 1.0	96.1 ± 3.1	89.1 ± 2.8
α_w (°)	57.6	60.3	45.0	45.8	40.7	84.6	82.7	78.7	73.6
C_1 (cm)	4.12 ± 0.28	8.07 ± 0.36	8.16 ± 0.41	11.98 ± 0.04	5.87 ± 0.12	3.79 ± 0.23	9.04 ± 0.36	8.50 ± 0.50	9.17 ± 0.16
C_t (cm)	16.12 ± 0.24	10.76 ± 0.32				13.99 ± 0.09	11.02 ± 0.21	6.13 ± 0.48	4.14 ± 0.12
y (cm)	0.89 ± 0.09	2.07 ± 0.14	2.93 ± 0.20	4.93 ± 0.74	6.17 ± 0.32	0.77 ± 0.08	1.73 ± 0.10	2.38 ± 0.17	2.18 ± 0.43
x (cm)	1.89 ± 0.17	2.79 ± 0.21	3.89 ± 0.22	4.31 ± 0.42	3.95 ± 0.27	1.96 ± 0.17	3.89 ± 0.53	3.90 ± 0.76	1.52 ± 0.47
w (cm)	2.11 ± 0.27	3.86 ± 0.31	5.22 ± 0.55	6.74 ± 0.49	4.76 ± 0.42	1.83 ± 0.32	3.65 ± 0.34	4.17 ± 0.29	2.59 ± 0.46
h (cm)	1.52 ± 0.11	3.59 ± 0.31	4.76 ± 0.45	6.89 ± 0.61	4.88 ± 0.45	1.38 ± 0.26	3.16 ± 0.27	3.95 ± 0.21	2.63 ± 0.41
w/h	1.83 ± 0.14	1.08 ± 0.05	1.10 ± 0.06	0.98 ± 0.05	0.98 ± 0.04	1.34 ± 0.15	1.16 ± 0.04	1.06 ± 0.07	0.98 ± 0.06
Δ_a (°)	70.4 ± 10.3	67.8 ± 9.6							
C_a (cm)	12.35 ± 1.33	14.11 ± 1.19							
Δ_a (°)[b]	64.2 ± 7.3								
C_a (cm)[b]	8.24 ± 0.56								

[a] α_w calculated as $\alpha_w = \alpha_t - \arctan\{[C_1 \sin(\alpha_t - \alpha_1)]/[C_t + C_1 \cos(\alpha_t - \alpha_1)]\}$.
[b] Secondary attachment streakline.

velocity increased quite evenly from 0.25 R to 0.50 R, with mean values of 21.9 cm s^{-1} and 44.2 cm s^{-1}, respectively. The maximum values of V_a were comparable to the mean velocity of the wing tip ($\approx$ 50 cm s^{-1}). Between 0.50 R and R, V_a was much more variable and tended to decrease (figure 6, table 2). The variability of V_a in the tip region may be attributed to separation and breakdown of the vortex core, as the leading-edge vortex merges into the tip vortex.

(*d*) *Circulation and lift-enhancement of the leading-edge vortex*

The circulation of the leading-edge vortex, Γ_{le}, at any cross-section is proportional to the swirl of the vortex, V_θ, and to its diameter, d (= the average of the vortex height and width):

$$\Gamma_{le} = \pi \cdot d \cdot V_\theta.$$

Under favourable circumstances, the helix angle of clearly defined streaklines in the leading-edge vortex could be measured (figure 3*c*, *d*). The average value of 15 measurements was 45.9° (standard deviation, SD ±11.9°), with no systematic spanwise changes. Assuming that the helix angle is 45°, the magnitude of the swirl, V_θ, is equal to the axial flow velocity, V_a (figure 6). Using the values of V_a for V_θ, the value of Γ_{le} could be calculated (table 2, figure 7*a*). The circulation, Γ_{le}, quadrupled from 0.25 R to 0.50 R. Further towards the wingtip the circulation remained constant or decreased, which is related to the process of vortex separation. Between $\phi = 30°$ and $\phi = 0°$ the circulation increased at all spanwise positions. At $\phi = -36°$, the circulation of the lower half of the vortex was virtually unchanged compared to that at $\phi = 0°$, but the circulation at 0.75 R had collapsed (figure 7*a*) since the vortex had separated there (see figure 4).

The sectional lift, L', (per unit span) of a wing is given by

$$L' = \rho V_w \Gamma,$$

where ρ is air density, V_w is the wing velocity and Γ is the circulation of the bound vortex. In these experiments we measured Γ_{le} and not Γ, which is the sum of the circulation of the boundary layer vorticity and Γ_{le}. By using Γ_{le} in the above equation we can therefore estimate the lift contribution, L_{le}', of the leading-edge vortex alone, which is also a lower limit for the total lift of the wing. The wing velocity, V_w, is the product of the angular velocity of the wing (averaged

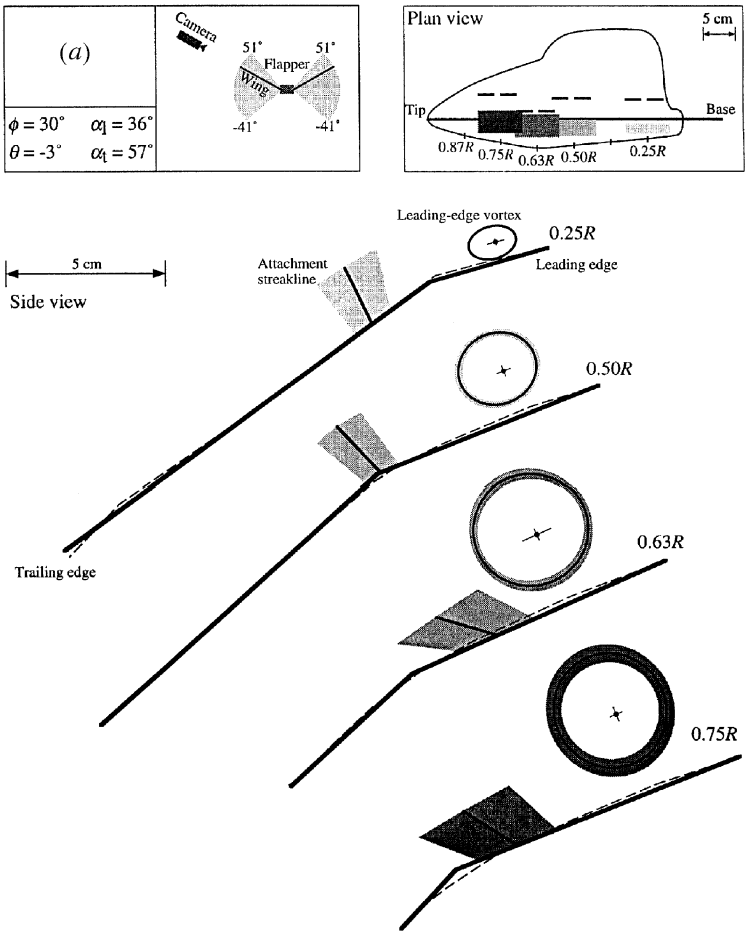

Figure 5 (*a*). For legend see p. 337.

over a time span of 0.16 s around the positional angle ϕ) and the spanwise position (table 2).

Spanwise, L_{le}' increased by a factor of eight from $0.25R$ to $0.50R$ and then stabilized (figure 7*b*, table 2). During the course of the downstroke, L_{le}' was quite similar at $\phi = 30°$ and $\phi = 0°$, but much reduced at $\phi = -36°$. The values at $\phi = 30°$ may seem high, considering the low circulation at that position, but this is compensated for by the larger velocities at $\phi = 30°$ than at $\phi = 0°$. Note that the lift force of the leading-edge vortex peaks sharply between $0.50R$ and $0.75R$ (figure 7*b*).

The total lift of the leading-edge vortex, L_{le}, is the integral of L_{le}' over the wing length, R; hence, the spanwise values were integrated trapezoidally along the wing length. Thus, L_{le} was estimated as 5.27 and 5.45 mN at $\phi = 30°$ and $\phi = 0°$, respectively, and as 1.74 mN at $\phi = -36°$ (table 2). The orientation of the lift force is approximately perpendicular to the stroke plane, supporting the insect's weight. The experimental hawkmoth of Willmott (1995) weighed 1.58 g (see §2*a*), requiring about 7.8 mN of lift per wing. It therefore follows that the leading-edge vortex can supply up to two-thirds of the required lift during the downstroke.

4. DISCUSSION

(*a*) *Dynamic stall or rotational lift?*

It is now well established that a leading-edge vortex with axial flow is present during hovering in the hawkmoth (Van den Berg & Ellington 1997; Willmott *et al.* 1997). With the detailed analysis presented in this paper, the aerodynamic mechanism responsible for creating this vortex can now be identified. The vortex can either have been generated during pronation and recaptured at the start of the downstroke (rotational lift mechanisms), or it can have been generated during the downstroke itself (dynamic stall). If a rotational mechanism is involved, the circulation of the vortex will be pre-established at the start of the downstroke. Furthermore, the circulation at any spanwise position, r, should be proportional to the square of the local chord, c^2. If dynamic stall is involved, however, the circulation will start to grow at the beginning of the downstroke, and the circulation will be proportional to the product, rc (Ellington 1984). We did not observe a leading-edge vortex at $\phi = 50°$ and hence there will be little if any circulation at the start of the downstroke. Figure 7*a* shows that for any spanwise position, the circulation increases dramatically until $\phi = 0°$, and then decreases as the wing starts to decelerate. Furthermore, the circulation varied along the span (figure 7*a*) much more like rc than c^2, which would have a circulation peak at the broad wing-

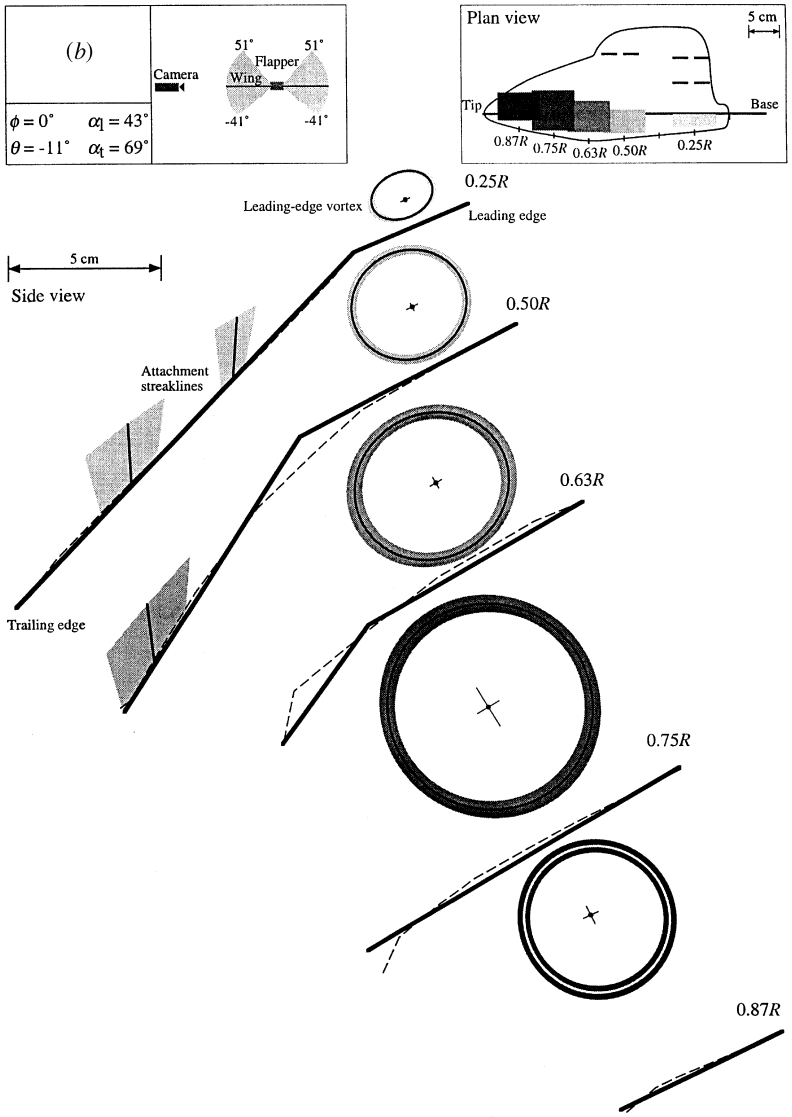

Figure 5 (*b*). For legend see opposite.

base. These results together show unequivocally that dynamic stall is responsible for the leading-edge vortex and certainly not rotational mechanisms.

(*b*) *The significance of the leading-edge vortex for hawkmoth hovering*

The high angles of attack of the wing led to the formation of a leading-edge vortex, which was stable along most of the wingspan during the entire downstroke. This vortex alone could contribute a lift force (L_{1e}) of up to two-thirds of the hawkmoth's weight (table 2). We assume that the results of the flapper can, at least as an approximation, be extrapolated to the hovering hawkmoth. The qualitative agreement between the vortex wake patterns and the quantitative match between the wake impulses for the flapper and the hawkmoth (Van den Berg & Ellington 1997) support this extrapolation.

Willmott (1995) found that a mean lift coefficient of 1.8 is required for weight support during hawkmoth hovering. If the leading-edge vortex can account for about two-thirds of the weight support, then the circulation of boundary layer vorticity must contribute another 0.6 to the lift coefficient. Willmott measured steady-state lift coefficients up to 0.6–0.7 for hawkmoth wings in a wind tunnel, so the additional 0.6 that is required falls just within the wing's capabilities. This approximation may well underestimate the leading-edge vortex lift of the hawkmoth, as it seems likely that the stability of the vortex is greater in the hawkmoth than in the flapper (see §4*d*).

(*c*) *The axial flow of the leading-edge vortex*

The potential of trapped or attached vortices for lift-enhancement has long been recognized in aerodynamics. A well-known application of a leading-edge vortex is the flow over the strongly swept wings of delta-winged aeroplanes. Polhamus (1966, 1971) showed that (depending on wing geometry and flight speed) the lift coefficient of the wings increased with an angle of attack up to about 25°, which is very high for an aeroplane, and reached a value of 1.2. Wu *et al.* (1991) give a detailed review of this subject and report maximum lift coefficients in the order of four to six. In a theoretical study, Rossow (1978) found lift coeffi-

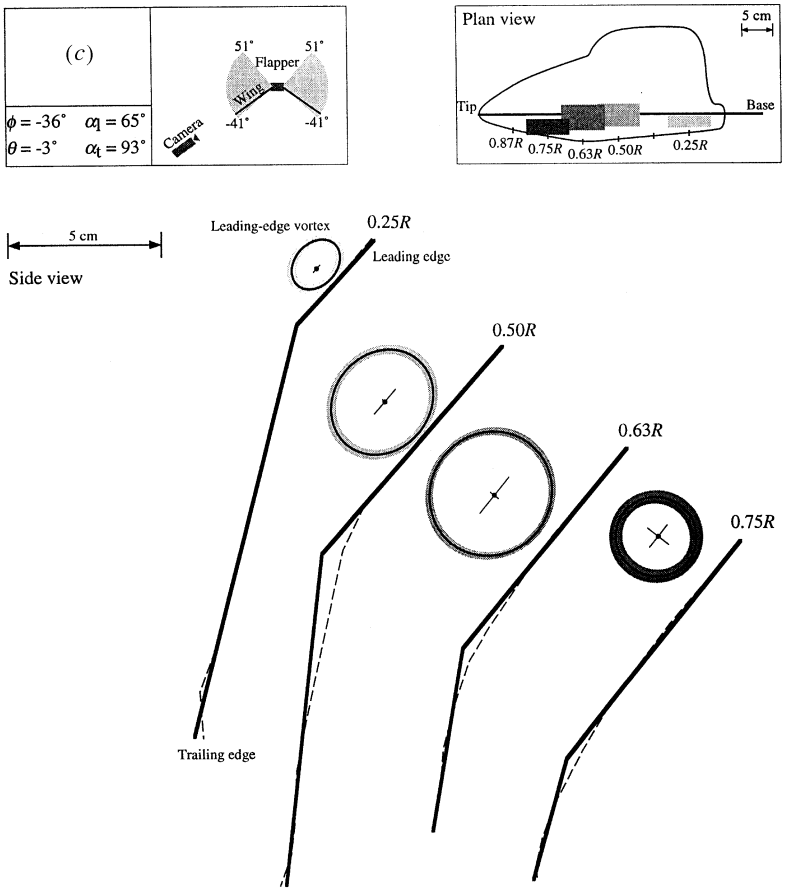

Figure 5. A graphical representation of the leading-edge vortex characteristics for (*a*) $\phi = 30°$, (*b*) $\phi = 0°$ and (*c*) $\phi = -36°$. The box on the top left shows the kinematic parameters of the wing position and the relative location of the camera. The box on the top right shows a plan view of the wing. The mean width of the leading-edge vortex and the mean position of the attachment streakline are indicated for each spanwise position. These positions are shown as 7 cm wide blocks, corresponding to the width of the light slice. In the side views, cross-sections of the wing are shown for each spanwise position in the orientation of the hovering hawkmoth. The elements in each cross-section represent the means of ten measurements of each parameter; the corresponding 95% confidence intervals (CI) are shown as hairlines and shaded areas. The mean length and angle of the leading- and trailing-edge sections are shown with thick lines, while the thin dashed line depicts an actual cross-sectional shape traced from a video frame. The leading-edge vortex is represented by an ellipse, showing its mean size and position and the 95% CI of its size. Note that the vortex is actually connected to the leading edge of the wing (see figure 4). The mean position of the centre of the leading-edge vortex is indicated by a dot. The mean position and angle of the attachment streaklines are indicated by a line joining the wing surface, while the shaded area shows the 95% CI of their position and angle.

Table 2. *The circulation,* Γ_{le}, *and spanwise lift,* L_{le}', *of the leading-edge vortex were estimated using the swirl velocity,* V_θ, *the mean vortex diameter,* d, *and the wing velocity,* V_w. *The swirl,* V_θ, *of the leading-edge vortex was assumed to be equal in magnitude to the axial flow velocity,* V_a

	V_w (cm s^{-1})	V_a (cm s^{-1}) (±s.e.)	V_θ (cm s^{-1})	d cm	Γ_{le} (cm^2 s^{-1})	L_{le}' (N cm^{-1}) $\times 10^{-6}$
$\phi = 30°$						
0.25R (0–0.38R)	24	21.9±2.5	21.9	1.28	88	25.9
0.50R (0.38–0.56R)	49	44.2±2.3	44.2	2.37	329	197
0.63R (0.56–0.69R)	61	29.2±3.0	29.2	3.58	328	245
0.75R (0.69R–R)	73	20.9±2.5	20.9	3.58	235	210
$\phi = 0°$						
0.25R (0–0.38R)	15	21.9±2.5	21.9	1.81	125	23.0
0.50R (0.38–0.56R)	31	44.2±2.3	44.2	3.72	517	196
0.63R (0.56–0.69R)	39	29.2±3.0	29.2	4.99	458	219
0.75R (0.69R–R)	46	20.9±2.5	20.9	6.81	447	252
$\phi = -36°$						
0.25R (0–0.38R)	7	21.9±2.5	21.9	1.60	110	9.4
0.50R (0.38–0.56R)	15	44.2±2.3	44.2	3.40	472	86.7
0.63R (0.56–0.69R)	18	29.2±3.0	29.2	4.06	372	82.0
0.75R (0.69R–R)	22	20.9±2.5	20.9	2.61	171	46.1

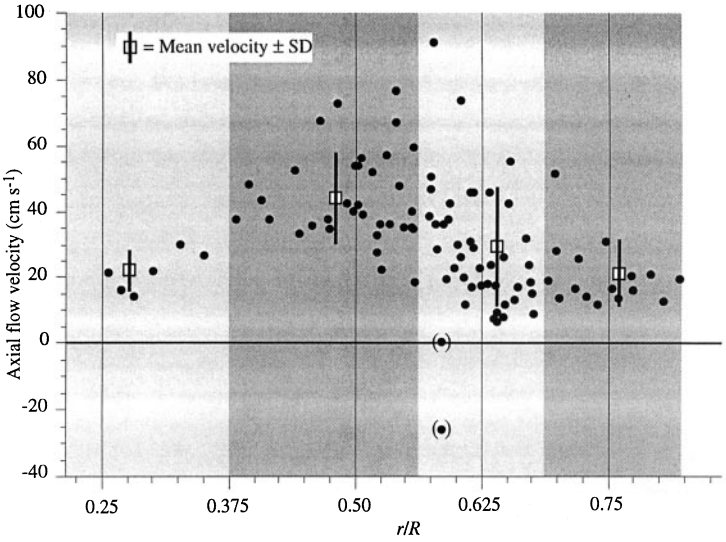

Figure 6. The axial flow velocity in the leading-edge vortex versus the spanwise position, r, on the wing, as a fraction of the wing length, R. The axial velocity was calculated from the movement of small 'smoke blobs' along the wing axis. The data are grouped in four spanwise sections, corresponding to the positions where the flow was studied ($0.25R$, $0.50R$, $0.63R$ and $0.75R$). The mean axial velocity and standard deviation for each section are indicated by a square and a vertical line. Two outliers (in parentheses) were omitted from the calculations.

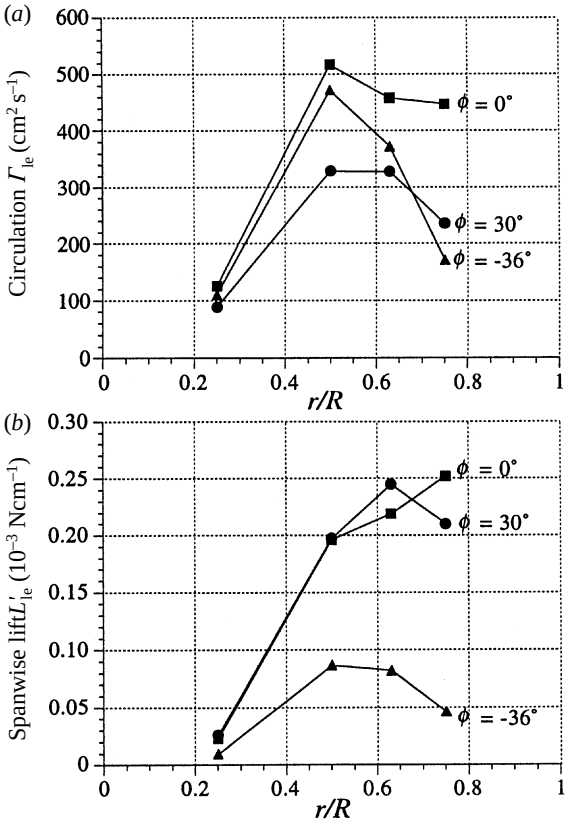

Figure 7. The estimated circulation (a) and lift force (b) of the leading-edge vortex as a function of the spanwise position, r, for three positional angles of the wing ($\phi = 30$, 0 and $-36°$).

cients up to ten when a vortex was trapped on an airfoil section using suction, but the stability of this vortex was marginal. Wu *et al.* (1991) emphasized that axial flow, induced by suction and/or swept wings, is essential for stability of a trapped vortex. The mechanism of vortex generation in delta wings, with stationary, swept wings, is quite different from that of hovering hawkmoths with flapping, non-swept wings, but there are clear similarities in the flow pattern of the leading-edge vortex. In a preliminary flapper experiment (almost without wing camber), we measured the size and position of the leading-edge vortex at $\phi = 0°$, halfway along the wing, as a function of the angle of attack (figure 8). Measurements of the leading-edge vortex of a delta wing over a range of angles of attack (Küchemann 1978) are strikingly similar (figure 8).

Axial flow in the leading-edge vortex has not been observed in previous two-dimensional experiments relevant to insect flight (Maxworthy 1979; Savage *et al.* 1979; Spedding & Maxworthy 1986; Dickinson & Götz 1993; Sunada *et al.* 1993; Dickinson 1994), but the spanwise pressure gradient necessary to drive the axial flow is, by definition, absent in two-dimensional studies. Maxworthy's (1979) three-dimensional model of the specialized fling motion is the only other case where axial flow has been reported. It therefore seems reasonable to assume that the flow is generated either by the dynamic pressure gradient associated with the velocity gradient along the flapping wing, and/or 'centrifugal' acceleration. However, axial flow has not been observed in the flow around helicopter rotors or wind turbine blades (McCrosky *et al.* 1976; De Vries 1983), although spanwise pressure gradients and 'centrifugal' accelerations must exist in these cases. It may be that the Reynolds numbers are too high for a significant leading-edge vortex to persist, or that the axial flow component is reduced in wings with a high aspect ratio like helicopter blades. The exact conditions for establishing axial flow in a leading-edge vortex in rotary wings are not yet understood.

(*d*) *Stability of the leading-edge vortex*

One of the main outstanding problems is the stability of the leading-edge vortex. In the flapper experiments the vortex core broke down as the vortex moved

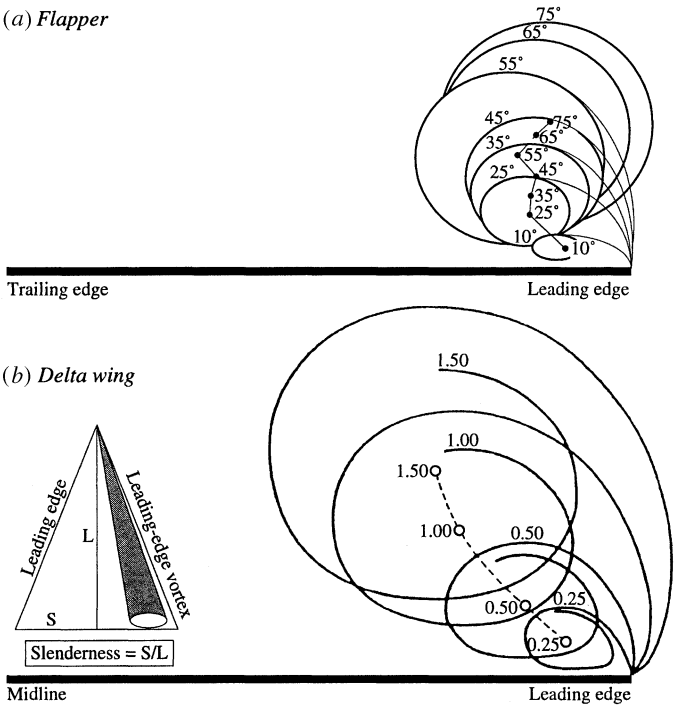

Figure 8. Comparison of the leading-edge vortex of the flapper with that of delta wings. (*a*) The results of early flapper experiments (without wing camber), where the angle of attack of the wing was varied from 10 to 75°. The size and position of the leading-edge vortex was measured at $0.50R$, $\phi = 0°$. (*b*) The size and position of the leading-edge vortex of a delta wing at different angles of attack. The numbers at the vortices are the angle of attack divided by the slenderness of the wing. The diagram on the left shows a plan view of a delta wing with a leading-edge vortex and the definition of the wing slenderness. Data for the delta wing from Küchemann (1978).

towards the wingtip, and soon after mid-downstroke, the vortex broke away from the wing surface between $0.63R$ and $0.75R$. A new, secondary vortex formed immediately where the initial one broke away, which once again confirms that the mechanism is dynamic stall. Note (figure 5, plan views) that at the spanwise position where separation occurs the leading edge curves backwards and the wing chord reduces considerably, which suggests that the position of vortex separation may be triggered (and controlled?) by details of the wing's construction. The exact moment of breakdown varied between wing beats (compare figure 3*a*, with no breakdown at $\phi = 0°$, to figure 3*c*, *d* with breakdown at $\phi = 0°$). Apparently, the leading-edge vortex is only marginally stable.

The stability of the vortex may well be better in the hovering hawkmoth than in the flapper. Since most of the lift force is generated in the distal half of the wing, just prior to vortex separation, even a slightly increased vortex stability would strongly increase the total lift produced by the wing. For optimal performance, the wingbeat kinematics of the hawkmoth should be 'designed' to postpone vortex separation as long as possible. Reduced vortex stability in the flapper due to gearbox vibrations or slightly incorrect wingbeat kinematics (see Van den Berg & Ellington 1997) may result in a noticeable reduction of the total lift force. The conditions for optimizing vortex stability are at present unknown. This is the most important outstanding question for future research, because vortex stability determines to what extent the lift-enhancement due to the leading-edge vortex can be exploited by insects. It is expected that the leading-edge vortex with strong axial flow, generated by dynamic stall, is not limited to the hovering hawkmoth, but will be employed by a wide range of insects during hovering and forward flight.

This work was supported by the SERC, the Hasselblad Foundation and an EC Human Capital and Mobility grant. Dr Berend Van den Berg is acknowledged for his comments on an earlier version of the manuscript.

REFERENCES

De Vries, O. 1983 On the theory of the horizontal-axis wind turbine. *A. Rev. Fluid Mech.* **15**, 77–96.

Dickinson, M. H. 1994 The effects of wing rotation on unsteady aerodynamic performance at low Reynolds numbers. *J. exp. Biol.* **192**, 179–206.

Dickinson, M. H. & Götz, K. G. 1993 Unsteady aerodynamic performance of model wings at low Reynolds numbers. *J. exp. Biol.* **174**, 45–64.

Ellington, C. P. 1984 The aerodynamics of hovering insect flight. IV. Aerodynamic mechanisms. *Phil. Trans. R. Soc. Lond.* B **305**, 79–113.

Ellington, C. P. 1995 Unsteady aerodynamics of insect flight. In *Biological fluid dynamics* (ed. C. P. Ellington & T. J. Pedley), *Symp. Soc. exp. Bio.* **49**, 109–129.

Grodnitsky, D. L. & Morozov, P. P. 1992 Flow visualization experiments on tethered flying green lacewings, *Chrysopa dasyptera*. *J. exp. Biol.* **169**, 143–163.

Grodnitsky, D. L. & Morozov, P. P. 1993 Vortex formation during tethered flight of functionally and morphologically two-winged insects, including evolutionary considerations on insect flight. *J. exp. Biol.* **182**, 11–40.

Kücheman, D. 1978 *The aerodynamic design of aircraft*. Oxford: Pergamon Press.

Maxworthy, T. 1979 Experiments on the Weis-Fogh mechanism of lift generation by insects in hovering flight. Part 1. Dynamics of the 'fling'. *J. Fluid Mech.* **93**, 47–63.

McCrosky, W. J., Carr, L. W. & McAllister, K. W. 1976 Dynamic stall experiments on oscillating airfoils. *AIAA Journal* **14**, 1.

Polhamus, E. C. 1966 A concept of the vortex lift of sharp-edge delta wings based on a leading-edge-suction analogy. *NASA Technical note* **3767**, 1–15.

Polhamus, E. C. 1971 Predictions of vortex-lift characteristics by a leading-edge suction analogy. *J. Aircraft* **8**, 193–199.

Rossow, V. J. 1978 Lift enhancement by an externally trapped vortex. *J. Aircraft* **15**, 618–625.

Savage, S. B., Newman, B. G. & Wong, D. T.-M. 1979 The role of vortices and unsteady effects during the hovering flight of dragonflies. *J. exp. Biol.* **83**, 59–77.

Spedding, G. R. & Maxworthy, T. 1986 The generation of circulation and lift in a rigid two-dimensional fling. *J. Fluid Mech.* **165**, 247–272.

Sunada, S., Kawachi, K., Watanabe, I. & Azuma, A. 1993 Fundamental analysis of three-dimensional 'near fling'. *J. exp. Biol.* **183**, 217–248.

Van den Berg, C. & Ellington, C. P. 1997 The vortex wake of a 'hovering' model hawkmoth. *Phil. Trans. R. Soc. Lond.* B **352**, 329–340.

Willmott, A. P. 1995 *The mechanics of hawkmoth flight*. Ph.D. thesis, University of Cambridge.

Willmott, A. P., Ellington, C. P. & Thomas, A. L. R. 1997 Flow visualization and unsteady aerodynamic mechanisms in the flight of the hawkmoth, *Manduca sexta*. *Phil. Trans. R. Soc. Lond.* B **352**, 303–316.

Wu, J. Z., Vakili, A. D. & Wu, J. M. 1991 Review of the physics of enhancing vortex lift by unsteady excitation. *Prog. Aerospace Sci.* **28**, 73–131.

Received 9 May 1996; *accepted 28 August 1996*

PHILOSOPHICAL TRANSACTIONS OF THE ROYAL SOCIETY B BIOLOGICAL SCIENCES